Microscopic description of the fission path with the Gogny interaction

J.-F. Lemaître* and S. Goriely
Institut d'Astronomie et d'Astrophysique, Université Libre de Bruxelles, Campus de la Plaine C.P. 226, BE-1050 Brussels, Belgium

S. Hilaire and N. Dubray
CEA, DAM, DIF, F-91297 Arpajon, France

(Received 7 May 2018; published 27 August 2018)

The Gogny D1M potential energy surfaces are used to extract the fission barrier of a large number of nuclei and to study in a systematic way the evolution of the fission barrier height depending on the proton and neutron numbers to deduce possible links with nuclear shell closures and are compared with evaluated nuclear data. The least-action paths are also computed, using Dijkstra's algorithm, and compared to the least-energy paths. Spontaneous fission half-lives are also calculated and compared with experimental data.

DOI: 10.1103/PhysRevC.98.024623

I. INTRODUCTION

The complexity of the fission process is well established, since it involves a many-body problem for which the interaction between nucleons is, in addition, not fully understood. Furthermore, nucleons move in such a way that they modify the system irreversibly and in depth, which raises dynamical issues. Since its discovery, fission has always been an active field of research regarding both its purely theoretical challenge and its practical applications. For some nuclear applications, such as energy production, nuclear waste management, and stellar nucleosynthesis, fission plays a key role. In particular, since the recent observation of the gravitational-wave event GW170817 of binary neutron-star mergers [1], the rapid neutron-capture process (or r-process) of stellar nucleosynthesis is now believed to take place in such an explosive neutron-rich environment. In this specific r-process scenario, the number of free neutrons per seed nucleus can reach a few hundred [2–4]. With such neutron richness, heavy fissioning nuclei can be produced. For this reason, at this astrophysical site, fission plays a fundamental role, more particularly, by (i) recycling the matter during neutron irradiation (or, if not, by allowing the possible production of superheavy long-lived nuclei, if any); (ii) shaping the r-abundance distribution in the $110 \leqslant A \leqslant 170$ mass region at the end of neutron irradiation; (iii) defining the residual production of some specific heavy stable nuclei, more specifically Pb and Bi, but also the long-lived cosmochronometers Th and U; and (iv) heating the environment through the energy released and consequently impacting the observed light curve of the astronomical event [3,4].

Fission probabilities remain, however, extremely difficult to predict and, consequently, the impact of the fission processes on the r-process nucleosynthesis complex to ascertain. In addition, it requires fission observables to be estimated for a few thousands nuclei, especially heavy exotic neutron-rich nuclei that cannot be produced in the laboratory. For practical applications, almost all existing calculations of the fission observables, such as neutron-induced, spontaneous, and β-delayed fission probabilities, rely on the multiple-humped fission penetration model, where fission barriers are described by inverted decoupled parabolas. Such approaches consider all ingredients as free parameters in order to be able to achieve more or less accurate fits to experimental cross sections [5]. Although such adjustments respond to the needs of some nuclear applications, their predictive power remains poor due to the large number of free parameters; these methods cannot be used in applications requiring a purely theoretical description of fission for experimentally unknown nuclei, such as nuclear astrophysics. For this reason, the prediction of fission probabilities is far from being satisfactory nowadays. Recent studies aim at providing sounder descriptions of some of the basic nuclear ingredients required to describe fission cross sections [3,6–9]. These concern, in particular, fission barriers (or, more generally, fission paths) and nuclear level densities at fission saddle points, but also fission fragment distribution, including the average number of emitted neutrons [10–12].

Detailed fission paths can nowadays be determined on the basis of the Hartree-Fock-Bogolyubov (HFB) model, which has proven its ability to estimate the potential energy surface (PES), and hence the static fission barrier heights and widths, with a relatively high degree of accuracy [6,8,9,13]. In this case, the static aspect of fission is treated via the least-energy path (LEP), from which the fission barrier is deduced, while the dynamical approach can be described through the least-action path (LAP) taking into account the inertia tensor.

In the present paper, we aim at providing updated calculations of fission observables for a large number of even-even nuclei in the framework of HFB calculations based on the D1M Gogny interaction [7]. In Sec. II, the HFB calculation of the PES is described, including corrections for effects beyond mean field and for triaxial deformations. In Sec. III, we focus

*jean-francois.lemaitre@ulb.ac.be

on the estimate of the least-energy fission path and study the sensitivity of the fission path and fission barrier heights with respect to different prescriptions for the beyond-mean-field collective corrections. We also compare the fission barrier heights deduced from the LEP to empirical data and carry out a systematic study of the fission barrier heights for all even-even nuclei from thorium ($Z = 90$) to darmstadtium ($Z = 110$) lying between the valley of β stability and the neutron dripline. In the second part of this article Sec. IV concerns the least-action fission path, with specific attention paid to the study of the inertia tensor and its impact on the least-action path, as well as the algorithm used to perform minimization of the action integral. In Sec. V, the least-energy and least-action fission paths are compared and in Sec. VI spontaneous fission lifetimes are estimated and compared with available experimental data. A sensitivity analysis is performed with respect to the impact of the treatment of the collective corrections beyond mean field. Finally, conclusions are drawn in Sec. VII.

II. POTENTIAL ENERGY SURFACE COMPUTATION

A. The Hartree-Fock-Bogoliubov method

The PES in the deformation space can be explored by imposing constraints on the standard HFB variational procedure [14–18] for a Hamiltonian $\hat{H}$ with respect to the various spatial degrees of freedom Q_{i0} to be explored. In the present work, we explore the axial quadrupole Q_{20} and octupole Q_{30} deformations only. The equations of motion are obtained by minimizing a Routhian,

$$E = \langle \Psi | \hat{H} - \lambda_N \hat{N} - \lambda_Z \hat{Z} - \sum_i \lambda_i \hat{Q}_i | \Psi \rangle, \quad (1)$$

where $|\Psi\rangle = |\Psi(Q_{20}, Q_{30})\rangle$ is the corresponding wave function at a given quadrupole Q_{20} and octupole Q_{30} deformation and the λ's the Langrange multipliers for the various constraints, which can be expressed as

$$\langle \Psi(Q_{20}, Q_{30}) | \hat{N} | \Psi(Q_{20}, Q_{30}) \rangle = N, \quad (2)$$

$$\langle \Psi(Q_{20}, Q_{30}) | \hat{Z} | \Psi(Q_{20}, Q_{30}) \rangle = Z, \quad (3)$$

$$\langle \Psi(Q_{20}, Q_{30}) | \hat{Q}_{i0} | \Psi(Q_{20}, Q_{30}) \rangle = Q_{i0}, \quad (4)$$

$$\langle \hat{Q}_{10} \rangle = \sum_{i=1}^{N+Z} \langle z_i \rangle = 0. \quad (5)$$

Equations (2) and (3) describe the constraints on the neutron N and proton Z numbers, Eq. (4) (with $i = 2, 3$) the constraints on the nuclear quadrupole Q_{20} and octupole Q_{30} deformation, and Eq. (5) ensures that the center of mass of the system is fixed at the origin of the coordinate system. The HFB wave functions are expanded on a basis corresponding to the union of two sets of deformed harmonic oscillator solutions shifted along the z axis. Each set of solutions consists of 11 major oscillator shells. This choice of 11 major shells leads to a "plateau condition." Every deformation parameter of this "two-center basis," including the distance between the two harmonic oscillator potentials, has been optimized for each HFB calculation by minimizing the HFB energy. More details can be found in Ref. [19]. A PES is represented on the (Q_{20}, Q_{30}) plane, where the quadrupole deformation Q_{20} is related to nucleus elongation and octupole deformation Q_{30} to mass (or left-right) asymmetry. All calculations in the present study are performed with the Gogny D1M interaction [7]. All details concerning HFB calculations with the Gogny interaction including the basis expansion, convergence criteria, and variational procedure can be found in Refs. [13,14,20], and references therein. The final PES on the (Q_{20}, Q_{30}) plane is constructed by correcting the mean-field energy $E_{\rm HFB}$ for the triaxial degree of freedom at small deformations and for the collective correlation effects beyond mean field, as described below.

B. Triaxial correction

It is well established that for small axial deformations, triaxial shapes can be favored, leading to a gain in energy of a few MeV with respect to the axial shape [13,21–24]. In particular, triaxiality is known to lower the inner fission barrier height by several MeV, so that the PES has to be corrected to take into account triaxial effects at low deformation, typically for $0 \leqslant Q_{20}[\mathrm{b}] \leqslant 100$. For a given quadrupole deformation, the triaxial correction $\Delta E_{\rm triax}(Q_{20})$ is given by

$$\Delta E_{\rm triax}(Q_{20}) = E_{\rm triax}(Q_{20}, 0) - \min_{\{Q_{22}\}}(E_{\rm triax}(Q_{20}, Q_{22})) \quad (6)$$

regardless of the octupole deformation. Triaxial calculations are obtained from the same constrained HFB method as Eq. (1) but with different constraints, i.e., quadrupole axial and triaxial (Q_{20}, Q_{22}) nuclear deformations instead of quadrupole and octupole (Q_{20}, Q_{30}) ones. More details can be found in Refs. [13,23,25]. Note that some recent relativistic mean-field studies even show that both nonaxial and reflection asymmetric shapes need to be considered simultaneously for the description of potential energy surfaces and, more particularly, the outer fission barriers [26]. However, such a conclusion has not yet been reached within the nonrelativistic mean-field approach.

C. Corrections beyond mean field

For a proper description of the fission process, in addition to the triaxial degree of freedom, correlations beyond the strict mean-field approach need to be considered, in particular, those stemming from high-amplitude collective motions [16,27]. The mean-field HFB energy at each quadrupole Q_{20} and octupole Q_{30} deformation has to be corrected to account for the collective correlations $\Delta E_{\rm ZPE}$ appearing in the collective Hamiltomian

$$\hat{\mathcal{H}}_{\rm coll} = -\frac{\hbar^2}{2} \sum_{ij=2,3} \frac{\partial}{\partial Q_{i0}} \frac{1}{B_{ij}} \frac{\partial}{\partial Q_{j0}} + E_{\rm HFB} - \Delta E_{\rm ZPE}, \quad (7)$$

where B_{ij} is the inertia tensor and $\Delta E_{\rm ZPE}$ the zero-point energy (ZPE) corrections. Only quadrupole collective coordinates are taken into account in the ZPE term of the collective Hamiltonian [Eq. (7)], describing the quadrupole component of the rotation, quadrupole vibration (β and γ), mode as defined in Ref. [25], i.e.,

$$\Delta E_{\rm ZPE} = \Delta V_{\rm vib} + \Delta V_{\rm rot} \quad (8)$$

$$= \sum_{i,j=0,2} \Delta V_{ij} + \Delta V_{-2-2} + \Delta V_{-1-1} + \Delta V_{11}, \quad (9)$$

where

$$\Delta V_{ij} = \frac{\mathcal{M}_{-2}^{ij}}{\mathcal{M}_{-3}^{ij}}, \tag{10}$$

$$\mathcal{M}_{k}^{ij} = \sum_{\mu\nu} (E_\mu + E_\nu)^k \left| \overline{q}_i^{\mu\nu} \overline{q}_j^{\mu\nu} \right|, \tag{11}$$

$$\overline{q}_i^{\mu\nu} = \langle \Phi_q | \eta_\mu \eta_\nu \hat{Q}_{2i} | \Phi_q \rangle, \tag{12}$$

η is the quasiparticle destruction operator, and $\hat{Q}_{2i}$ the quadrupole operator. Two methods to describe such correlations have been adopted here, namely, the generator coordinate method (GCM), optimizing in a variational approach the multiconfigurational mean-field states, and the cranking approximation to the adiabatic time-dependent Hartree-Fock (ATDHF) approach in the limit of low velocities and high amplitudes. More details about zero-point energy corrections and inertia tensor derivation can be found in Refs. [14,18,25,27,28].

III. LEAST-ENERGY FISSION PATH

A. Flooding model

The method used to determine the LEP of a PES is inspired by the flooding method developed in Ref. [29] used to extract the saddle point connecting two wells. It consists of filling a well until it overflows, this overflow point corresponding to the saddle point. As a PES is a set of points distributed over a regular (Q_{20}, Q_{30}) mesh, a step-by-step method is used. Starting from the lowest well, known as the first "wet" point, the "water level" E (or flooding level) is gradually increased until it overflows over a saddle point. To determine precisely the location (Q_{20}, Q_{30}) of a saddle point using a constant level increment δE, however, requires a fine deformation grid as well as a small energy increment and, hence, a significant computing time. In order to optimize this computation time, the water - increment is not taken as a constant but rather determined through the so-called "dry" neighbors. The increment δE is thus equal to the difference between the current water level and the lowest point among all dry neighbors in the wet area. Doing so, this point is automatically included in the wet area, which reaches the level $E + \delta E$. If there is a point among the dry neighbors below the water level (this point trivially becomes wet), it implies that a saddle point has just been overflowed. This saddle point is then the penultimate point included in the wet area.

A simple way to determine the LEP consists of computing it iteratively, starting from the ground-state well. A saddle point S_x is obtained by flooding the well W_x; the next well W_{x+1} is located by the steepest descent from the newly obtained saddle point. This procedure is repeated until the right part of the PES corresponding to the fusion valley is reached. To prevent from backtracking to a previously determined well W_x via a saddle point recently found, S_x, the flooding is restricted to the area such that Q_{20} is greater or equal to the Q_{20} of the new well W_{x+1}. It is equivalent to building a "dam" along the Q_{30} deformation passing through the W_{x+1} point before flooding the corresponding well.

However, this iterative method fails in some cases due to the presence of a shape isomer, an octupole one as illustrated for $^{260}_{100}\mathrm{Fm}_{160}$ in Fig. 1. This shape isomer issue leads to a discontinuous LEP and/or a pseudo saddle point. Starting from the ground-state well W_1 (see Fig. 1), the flooding procedure detects the saddle point S_1. This point connects the flooded areas $E < E_{S_1}$ and $E \leqslant E_{S_1}$, related to the first W_1 and second W_2 wells, respectively. It should be noted that the $E < E_{S_i}$ area contains points before overflowing the well W_i, and the $E \leqslant E_{S_i}$ area contains only new points beyond the saddle point S_i once S_i has been overflowed. From W_2, the iterative flooding procedure cannot detect the saddle point S_2 because it is located in the forbidden area delimited by the "dam" built along the Q_{30} deformation passing through the W_2 (dotted gray line in Fig. 1). Therefore, the next detected saddle point is the point labeled X in Fig. 1. However, X is not a true saddle point but a pseudo one created by the restriction of the flooding area thanks to the dam. Consequently, the LEP finally obtained

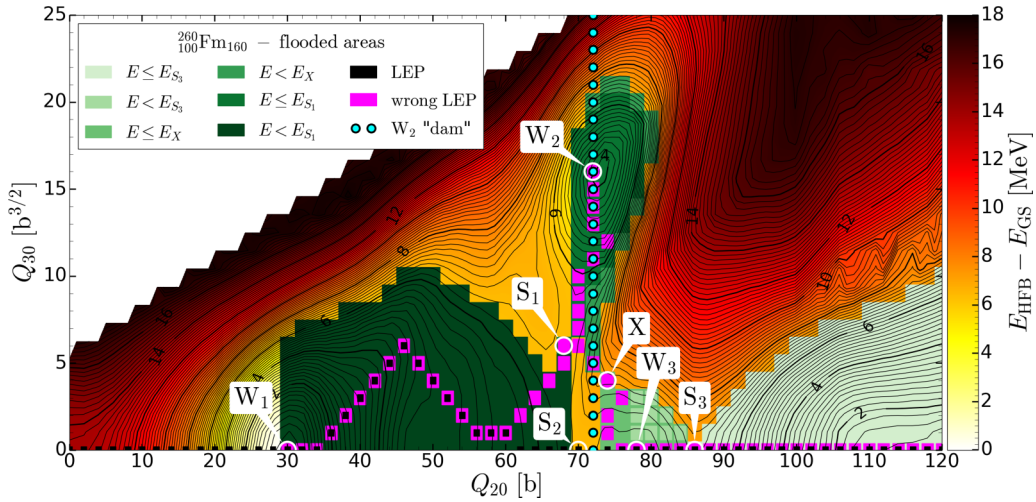

FIG. 1. Illustration of the shape isomer issue, located at W_2, when applying the flooding procedure to the PES of $^{260}_{100}\mathrm{Fm}_{160}$. Due to this shape isomer, the iterative flooding method leads to an incorrect LEP (magenta squares) with a dead-end from S_1 to W_2 and a pseudo saddle point X. The LEP obtained with the comprehensive BST approach (black squares) has no pseudo saddle point. The $E < E_{S_3}$ area is included in the $E \leqslant E_X$ area because the well W_3 is the latter area.

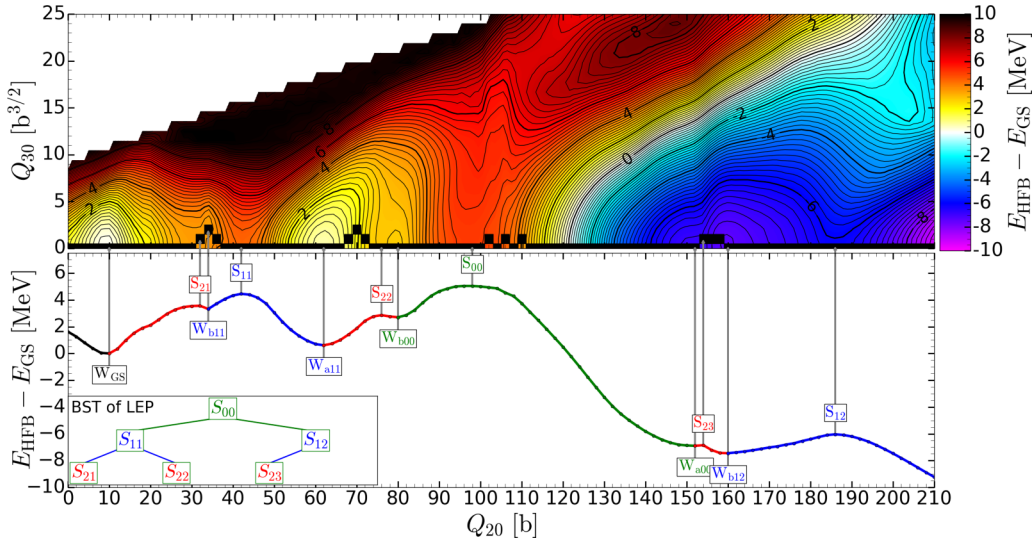

FIG. 2. Illustration of the LEP determination by the BST method for $^{286}_{106}$Sg$_{180}$. The search starts with the computation of the highest saddle point of the LEP S_{00} (00 means that it is the first saddle-point search). After that, the LEP computation is reduced to two subproblems. Their resolutions give S_{11} and S_{12}; the first index corresponds to the first dichotomy, and the second to the number of the subproblem starting from the ground state. $W_{\rm bxx}$ and $W_{\rm axx}$ are wells before and after the saddle point $S_{\rm xx}$ obtained by the steepest descent from the latter. The ground-state well $W_{\rm GS}$ is determined by the steepest descent from point (0,0). Inset: BST built during the saddle-point search.

for $^{260}_{100}$Fm$_{160}$, due to the creation of this pseudo saddle point connects (W_1–S_1–X–W_3–S_3) and a dead end: (S_1–W_2).

To avoid such drawbacks, a more comprehensive approach is needed. This approach is based on a binary search of LEP saddle points using the so-called binary search tree (BST) data structure [30]. The first step of this algorithm, illustrated in Fig. 2, is to find the saddle point which connects the ground state $W_{\rm GS}$ to the right part of the PES corresponding to the fusion valley using the flooding method. This saddle point is the highest saddle point S_{00} of the LEP which also defines the primary (i.e., the highest) fission barrier. From this saddle point, the well before W_{b00} and after W_{a00} the saddle point S_{00} are determined by the steepest descent method, which also determines the part of the LEP between W_{b00} and W_{a00} (green part of the LEP in Fig. 2). From there on, the problem is divided into two subproblems: on the one hand, to find the highest saddle point S_{11} between $W_{\rm GS}$ and W_{b00} and, on the other hand, to find the highest saddle point S_{12} between W_{a00} and the fusion valley. The resolution of these two subproblems gives the blue parts of the LEP in Fig. 2. The BST (see also the inset in Fig. 2) is completed by adding two new nodes related to S_{11} and S_{12}, each of them containing necessary information for the final reconstruction of the LEP. The saddle-point search between two wells is stopped when they correspond to the same point, and the LEP is complete when all parts are connected. Its reconstruction is done through an in-order search [30] of the BST, which gives the saddle points in good order, from the ground state to the fusion valley. In the example in Fig. 2, this sequence of saddle points is given by S_{21}, S_{11}, S_{22}, S_{00}, S_{23}, S_{12}.

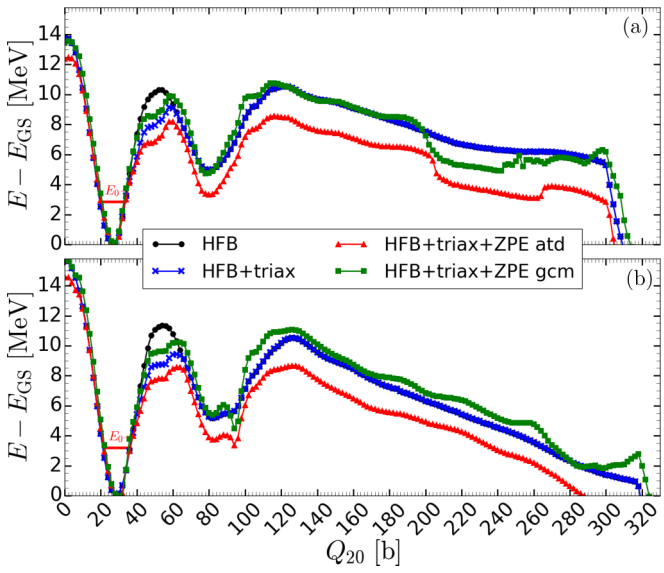

FIG. 3. LEP projected on the Q_{20} axis for (a) $^{236}_{92}$U$_{144}$ and (b) $^{240}_{94}$Pu$_{146}$ with different corrections: no corrections, triaxial, and triaxial + ZPE in the ATDHF framework and in the GCM framework for collective corrections.

B. Impact of the triaxial and collective corrections on the fission path

As mentioned in Sec. II B, the triaxial energy correction (HFB + triax) is known to impact the LEP, especially for $0 \leqslant Q_{20}$[b] $\leqslant 100$, and tends to decrease the height of the inner fission barrier [9,13,23,24]. For $^{236}_{92}$U$_{144}$ and $^{240}_{94}$Pu$_{146}$, the triaxial correction occurs around $40 \leqslant Q_{20}$[b] $\leqslant 70$ (see Fig. 3). In the plutonium case [Fig. 3(b)], the inner one is the fission barrier for raw PES but the triaxial correction reduces the inner barrier such that the outer barrier becomes the highest one. The impact of collective corrections depends on the method used to compute them. The GCM correction has a moderated impact on the fission path because it weakly

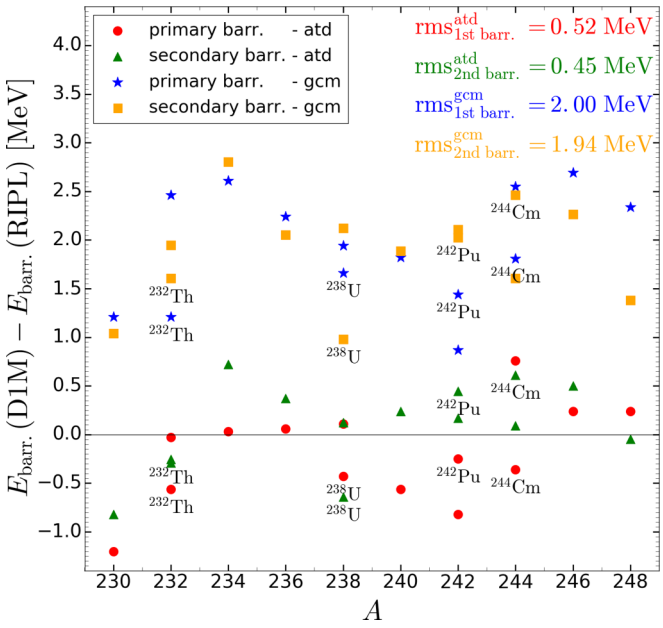

FIG. 4. Comparison of D1M primary and secondary fission barrier height in the ADTHF and GCM frameworks with the empirical values [31] for $^{230-232}$Th, $^{232-238}$U, $^{238-244}$Pu, and $^{242-248}$Cu. The rms of the primary fission barrier is equal to 0.52 MeV for the ATDHF framework and 2 MeV for the GCM one. The rms of the secondary fission barrier is equal to 0.45 MeV for the ATDHF framework and 1.94 MeV for the GCM one. For isobaric nuclei, one of the names is displayed below its corresponding symbol.

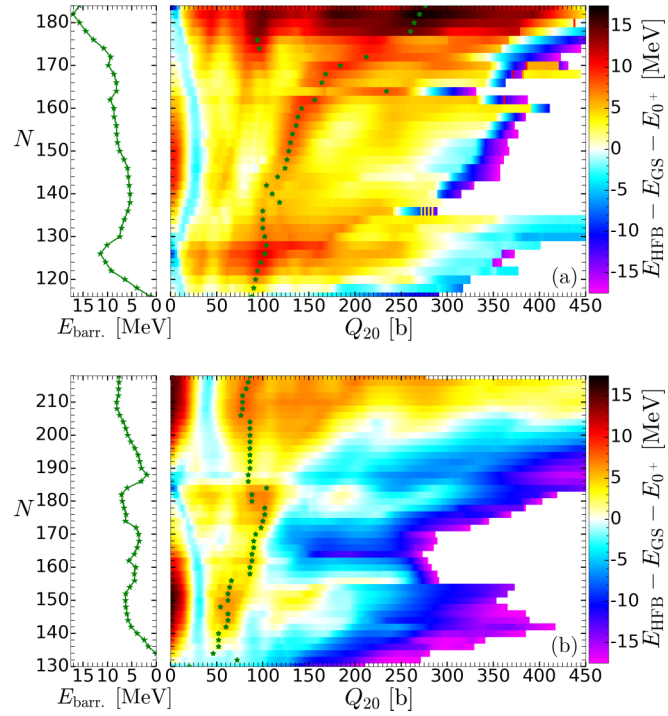

FIG. 5. Color representation of the LEP for (a) U and (b) Fm isotopes (b). Green stars represent the location of the highest barrier along each LEP. The left panels represent the fission barrier height for the whole isotopic chain with respect to the corresponding 0^+ level.

varies with the Q_{20} constraint. In the uranium and plutonium cases, the difference in the GCM correction between the one at the fission barrier and the one in the ground state is less than 0.2 MeV and acts like a global energy shift on the PES. More precisely, it slightly increases the inner and outer fission barrier height compared to the fission path without collective correction. The ATDHF correction has a more important impact on the PES topology, in particular, on the fission barrier height. This correction increases with the Q_{20} constraint from the ground state to the outer fission barrier. The difference is around 2 MeV between the ground state and the fission barrier: the ATDHF correction reduces the fission barrier height by 2 MeV.

C. Fission barriers of experimentally known nuclei

The fission barrier heights of particular interest in nuclear applications can be extracted directly from the LEP, since they correspond to the various saddle points with respect to the ground-state 0^+ level. More specifically, the fission barriers are determined in a way similar to the so-called Method A in Ref. [13], i.e.,

$$E_{\mathrm{barr}} = E^{\mathrm{saddle}}_{\mathrm{HFB}} - \Delta E^{\mathrm{saddle}}_{\mathrm{triax}} - \Delta E^{\mathrm{saddle}}_{\mathrm{ZPE}} - E_{0^+}, \qquad (13)$$

where E_{0^+} corresponds to the ground-state energy within the five-dimensional collective Hamiltonian framework [7,13,25]. Each saddle point gives rise to a fission barrier, the highest (or primary) barrier being crucial for the calculation of fission probabilities.

In Fig. 4, we compare the primary barrier height of the 14 even-even nuclei for which empirical values have been extracted from fission cross-section measurements [31]. Both the ATDHF and the GCM approximation of the collective correction energies have been considered in this comparison. In the case of the ADTHF correction, an excellent agreement is found with empirical data with the root-mean-square (rms) deviation of 0.52 MeV. The agreement is particularly good for ^{232}U, ^{234}U, ^{236}U, and ^{238}Pu. The rms is 1.48 MeV higher in the case of the GCM correction. This difference is due to the variation of the ATDHF correction with the Q_{20} coordinate, whereas the GCM one is almost constant as mentioned in Sec. III B. For comparison, in the same data set, an rms deviation of 0.75 MeV is obtained with the Skyrme-HFB calculation based on the BSk14 force [6] as well as with the finite-range liquid-drop model [32]. The lower rms deviation of 0.35 MeV is obtained with the multidimensional constrained relativistic mean-field model [26].

D. Large-scale calculation of fission barriers

We now calculate the primary fission barriers from the LEP for all 500 even-even nuclei with $90 \leqslant Z \leqslant 110$ lying between the D1M proton and the neutron driplines. We show in Fig. 5(a) the LEP of U isotopes. The vertical blue strip on the left corresponds to the location of the 0^+ ground state. The arch pattern observed is due to shell effects, in particular, the spherical ($Q_{20} = 0$) shell closure at $N = 126$ and $N = 184$. In the U case, the quadrupole deformation at the primary fission barrier is seen to increase significantly with N, from $Q_{20} = 90$

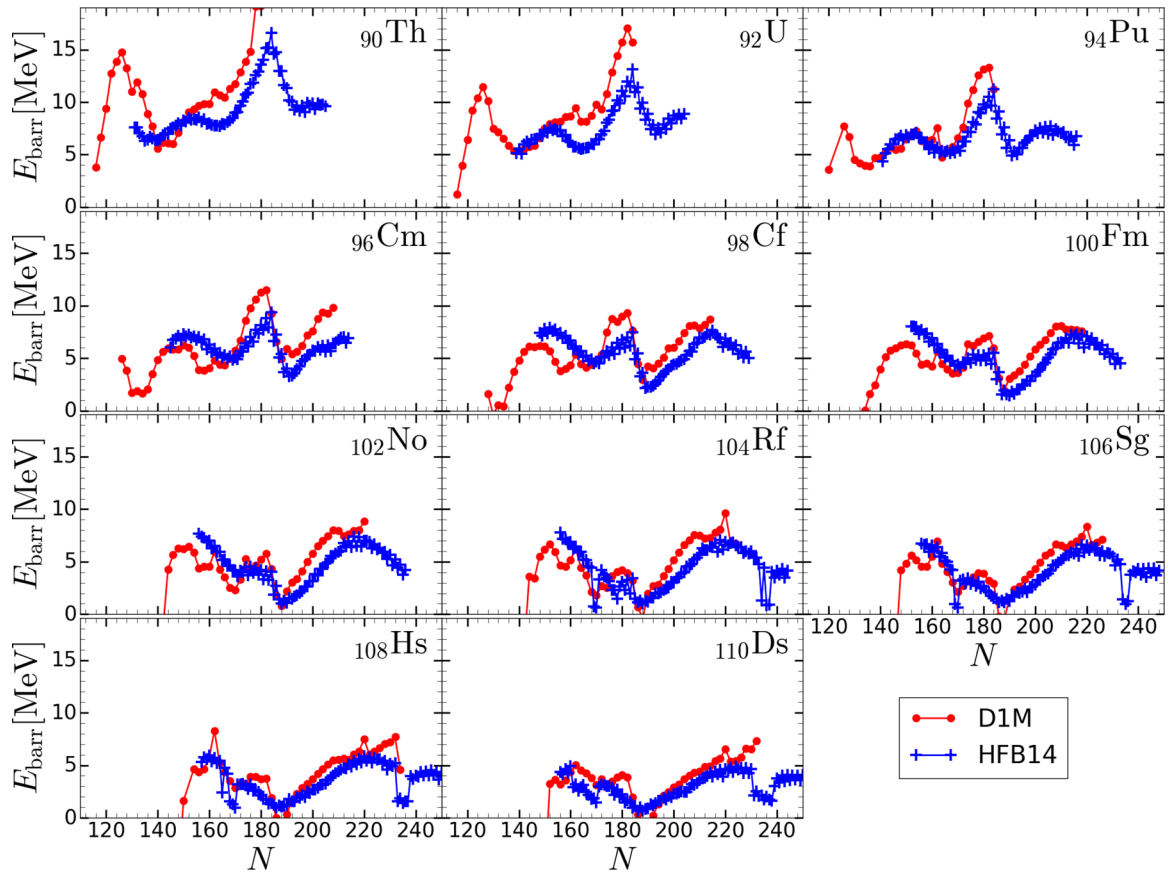

FIG. 6. Height of D1M primary fission barriers compared with HFB14 ones [6] for all even-even nuclei with $90 \leqslant Z \leqslant 110$ lying between the D1M proton and the D1M neutron driplines.

b for ^{208}U to $Q_{20} = 270$ b for ^{276}U. The fission barrier heights remain between 5 and 10 MeV for $N \in [130, 170]$ [Fig. 5(a)] but vary quite rapidly in the vicinity of a shell closure, reaching a maximum of 17 MeV around the neutron shell closure at $N = 184$ and of some 12 MeV around $N = 126$.

A similar pattern is found for the Fm isotopes [Fig. 5(b)], with the ground-state 0^+ level showing also an arch structure linked to the $N = 184$ shell closure. The quadrupole deformation of the primary barriers lies between 40 and 110 b and is consequently less spread than in the U case. In particular, the neutron shell closure does not impact significantly the deformation of the fission barrier (around $Q_{20} = 80$–90 b) but, rather, its height, which drops to a few MeV at $N = 188$, just after neutron shell closure $N = 184$, where a local maximum is reached (Fig. 5, lower left panel).

In both cases, the primary barrier height becomes negligible for neutron-deficient nuclei close to the proton dripline. This means that such nuclei are highly unstable against spontaneous fission.

The fusion valley, which corresponds to the blue-pink zone at large quadrupole deformations in Fig. 5, appears at lower Q_{20} values for Fm isotopes in comparison with U isotopes. Primary fission barriers are globally lower for Fm isotopes.

We then compare in Fig. 6 our D1M primary barriers with those obtained within the Skyrme HFB framework with the BSk14 interaction (the so-called HFB-14 mass model) [6]. Globally, D1M barriers are higher than HFB14 ones, particularly around $N = 184$. This is due to the stronger shell effect (and lower effective mass) obtained with D1M in comparison with BSk14. In some cases, the fission barrier drops to 0 when the 0^+ ground state is higher than the highest fission saddle point; this is the case, for example, for $^{188}_{106}$Sg$_{294}$, $^{188}_{108}$Hs$_{296}$, or $^{188}_{110}$Ds$_{298}$. These nuclei are unstable against spontaneous fission.

In Fig. 7, the height as well as the quadrupole and octupole deformation of the D1M fission barriers for all calculated PES is represented on the (N, Z) plane to highlight the proton and neutron influence, through shell closure, on fission barriers. The nucleus proton number has a weak impact on the fission barrier height, the main effect being that the fission barrier height decreases with the proton number. Contrary to the proton number, the neutron number has a stronger impact. For example, nuclei having around 188 neutrons have a low fission barrier, equal to 0 in some cases for $Z \geqslant 104$. Nuclei with $Z \leqslant 98$ and $N \approx 178$ show a high fission barrier, reaching more than 10 MeV.The proton dripline nuclei have no fission barrier because the ground-state well is not deep enough to have a bound 0^+ state.

In Figs. 7(b) and 7(c), we illustrate the reduced quadrupole deformation $\tilde{q}_{20} = Q_{20}/AR_0^2$ (where the radius parameter $R_0 = 1.2A^{1/3}$ fm is adopted) and reduced octupole deformation (or mass asymmetry) $\tilde{q}_{30} = Q_{30}/AR_0^3$ of the primary

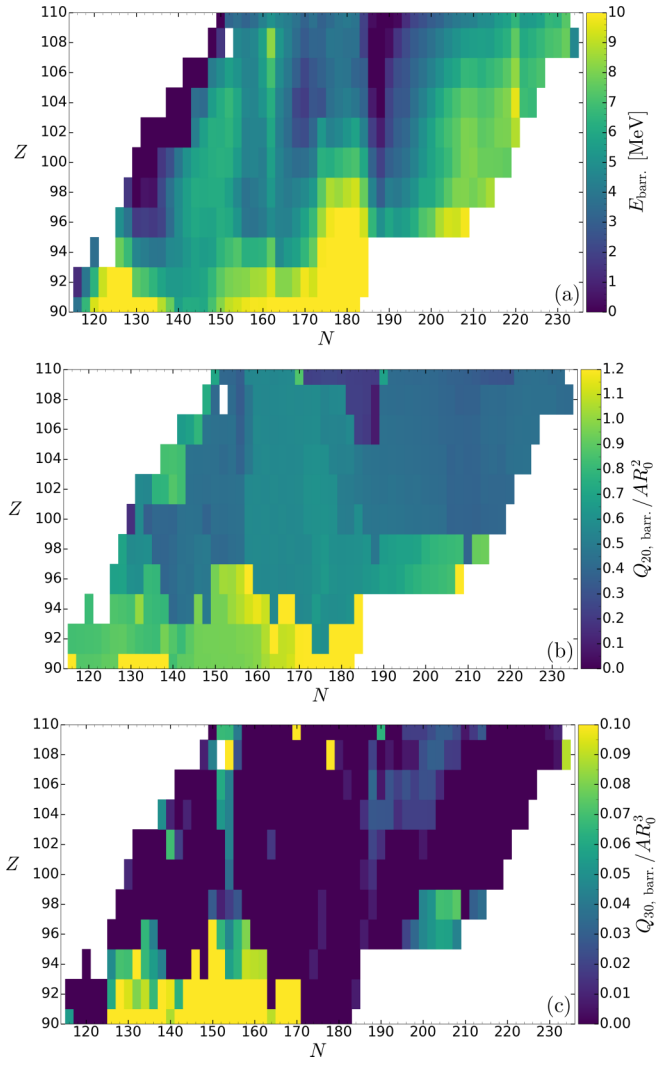

FIG. 7. Color representation in the (N, Z) plane of D1M fission barrier properties: (a) barrier height, (b) reduced quadrupole deformation $\tilde{q}_{20}$, and (c) reduced octupole deformation $\tilde{q}_{30}$.

fission barriers. No particular dependence of the quadrupole elongation on the proton or neutron number is found except that the elongation tends to increase as a function of N (see also Fig. 5 for U and Fm isotopes). Concerning the mass asymmetry, for most of the nuclei, the highest barriers are left-right symmetric, i.e., $\tilde{q}_{30} \simeq 0$, except for $Z \lesssim 96$ and $130 < N < 170$ nuclei with $\tilde{q}_{30} \gtrsim 0.1$ and a primary (heighest) barrier corresponding to the outer one with a large quadrupole deformation.

IV. LEAST-ACTION FISSION PATH

The LEP corresponds to a static approach without any dynamical consideration, whereas the LAP takes into account some dynamical aspects of the fission process, in particular, the inertia evolution along a given path. In the case of spontaneous fission, the shortest path is the one which maximizes the probability of penetration through the barrier by the tunneling effect. This probability P can be calculated in the semiclassical WKB approximation [33,34],

$$P = \frac{1}{1 + e^{2S(E)/\hbar}}. \tag{14}$$

To maximize the penetration probability, the action defined by [33,34]

$$S = \int_{\rm ITP}^{\rm OTP} \sqrt{2\mu(x)(V(x) - E)}dx \tag{15}$$

has to be minimized. In Eq. (15), $V(x)$ is the potential energy of the system, $\mu(x)$ the effective inertia, E the total energy of the system (which depends on its excitation energy), and x the curvilinear coordinate of the LAP ($x = 0$ corresponding to the ground state); ITP stands for the inner turning point close to the ground-state well, and OTP for the outer turning point located in the right part of the PES (high Q_{20}). When not mentioned, the excitation energy of the system corresponds to the energy of the 0^+ ground state, the same one used in Eq. (13), which is obtained by solving the five-dimensional collective Bohr Hamiltonian [7]. The dynamical aspect is contained in the effective inertia $\mu(x)$ at a given point (Q_{20}, Q_{30}) of the PES, which depends on the Q_{20} and Q_{30} deformations but also on the direction of the path at this point. The LAP corresponds to the path for which spontaneous fission is the most likely, i.e., the action is minimal.

The effective inertia $\mu(x)$ is the projection of the inertia tensor B_{ij} along the path considered and can be expressed as [8,9,33–35]

$$\mu(x) = \sum_{ij=2,3} B_{ij}(Q_{20}, Q_{30}) \frac{dQ_{20}}{dx} \frac{dQ_{30}}{dx}. \tag{16}$$

For a path on the (Q_{20}, Q_{30}) plane, the tensor components B_{22}, B_{23}, and B_{33} associated with the quadrupole and octupole modes need to be determined. The different tensor components are calculated with the GCM and ATDHF method using the cranking approximation [8,9,18,25,36]. A comparison between ATDHF and GCM inertia tensors is discussed in Sec. IV B.

A. Minimization of the action

Dijkstra's algorithm [37] is used to compute the LAP. This algorithm, based on graph data structure, finds the shortest path between a starting point, i.e., the source of the graph, and every other point (or nodes) in the graph. A tree data structure containing the shortest paths between the starting point and all points in the graph is built by progressively exploring the graph. Thanks to this progressive exploration, Dijkstra's algorithm gives the exact solution and does not need a final point, contrary to the dynamic-programming method or Ritz method used in Ref. [33]. However, it is possible to define a stop condition to avoid calculating unnecessary paths. When this stop condition is reached, the shortest path is obtained by backtracking from this point to the starting point using tree data structure. In the case of LAP computation, the starting point is the ground state of the nuclei, the graph corresponds to the PES in the deformation plane, and the stop condition is when an outer turning point is reached, i.e., the scission or outer turning line of the PES, defined as $V - E = 0$. The distance

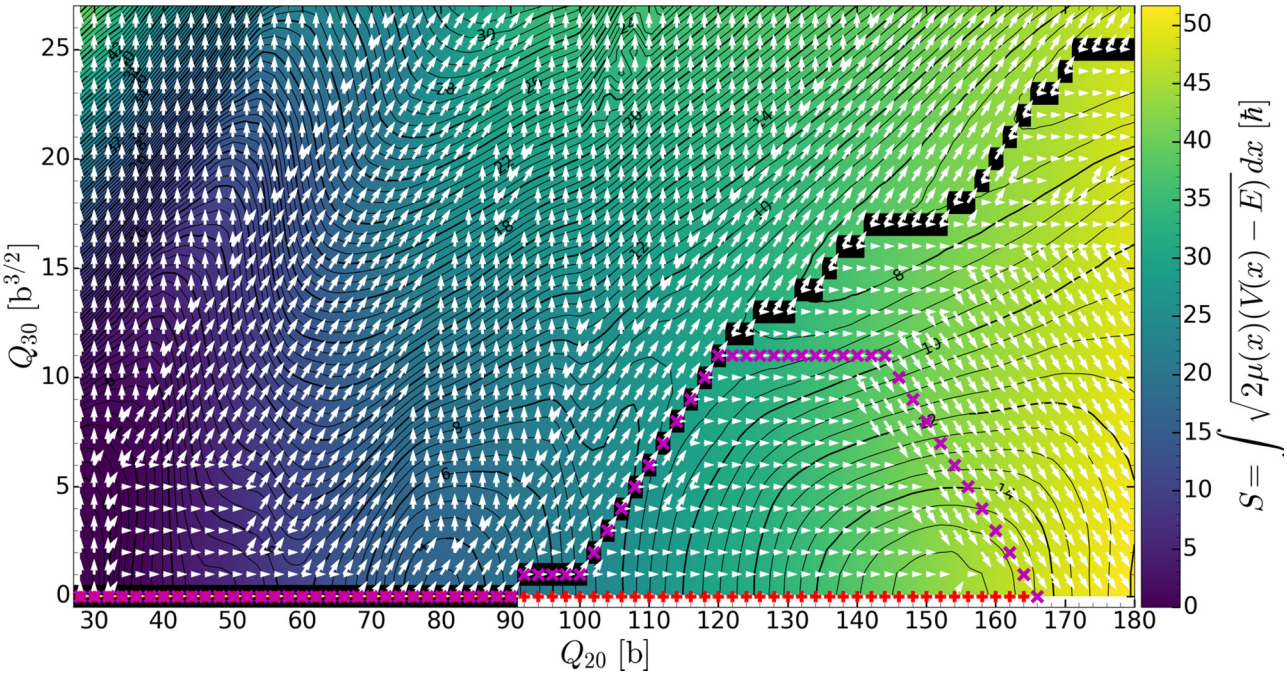

FIG. 8. Evolution of the tree data structure, represented by white arrows, during the LAP computation of ^{236}U for an initial excitation energy $E^* = E_{0^+}$. Black lines represent isoenergies of the PES, and the color scale is the action of the path between the ground state and the various points of the PES. The LAP is shown byh black squares. The scission line is not represented here. The LAP from ground state to $(Q_{20}[\text{b}], Q_{30}[\text{b}^{3/2}]) = (164, 0)$ is represented by red plus symbols, while the LAP from ground state to (166,0) is depicted by the magenta x's.

between a given point $(Q_{20,i}, Q_{30,i})$ and a neighboring point $(Q_{20,i+1}, Q_{30,i+1})$ is defined by

$$dS = \sqrt{2\mu(Q_{20,i}, Q_{30,i}, Q_{20,i+1}, Q_{30,i+1})} \times \sqrt{V(Q_{20,i}, Q_{30,i}) - E}\, dx, \quad (17)$$

where the effective inertia $\mu(Q_{20,i}, Q_{30,i}, Q_{20,i+1}, Q_{30,i+1})$ depends on the location of the point $(Q_{20,i}, Q_{30,i})$ and the direction of the point $(Q_{20,i+1}, Q_{30,i+1})$ relative to the point $(Q_{20,i}, Q_{30,i})$. It should be mentioned that the areas $E > V$, like shape isomers, can be explored but they do not contribute to the action [Eq. (15)] since there is no tunnel effect in this region. For this reason, in the vicinity of a well, the distance between two neighboring points [Eq. (17)] can be set to 0 and the Q_{20} direction is favored. During the exploration procedure of the LAP, only the unexplored neighbors of a given point are considered. The resulting exploration tree is represented in Fig. 8.

In some cases, two neighboring points can be reached through different paths even if the actions of both LAPs are almost equal. Such an example is illustrated in Fig. 8, where the $(Q_{20}[\text{b}], Q_{30}[\text{b}^{3/2}]) = (164, 0)$ and (166,0) deformations can be reached by two different paths for $Q_{20} > 90$ b, the first one following the Q_{20} axis and the second one passing through the saddle point at (120,11).

B. Impact of the inertia tensor on the fission path

The collective corrections calculated using either the ATDHF or the GCM framework affect not only the energy along the fission path but also the inertia tensor. For consistency, these two quantities are computed within the same framework. The case of ^{236}U is considered to study the impact of the ATDHF and GCM frameworks on the LAP (Fig. 9). It is not possible to know *a priori* whether the action along the LAP will be lower in the ATDHF or the GCM framework because the LAPs projected on the (Q_{20}, Q_{30}) plane, i.e., $Q_{30}(Q_{20})$, are similar [Fig. 9(a)]. The energy $E(Q_{20})$ and inertia $\mu(Q_{20})$ contributions to the action and the LAP can play a different role and behave differently depending on the framework adopted. As shown in Figs. 9(a) and 9(b), a higher energy contribution with the GCM corrections can be compensated by a lower inertia, with respect to the ATDHF framework. However, the shape of the $E(Q_{20})$ and $\mu(Q_{20})$ functions is seen not to be drastically affected by the framework used. The two distances differ only for $Q_{20} > 220$ b, where $dS_{\text{GCM}} > dS_{\text{ATD}}$ due to the weaker collective correction in the GCM framework. The final action of the ATDHF LAP is equal to 63.6$\hbar$, while the GCM LAP is equal to 66.7$\hbar$, slightly higher than the ATDHF one [Fig. 9(c)].

To complete this study, the ^{236}U LAP is also computed with the semiempirical (SEMP) constant, and widely used, effective inertia, defined as [38]

$$\mu_\epsilon^{\text{SEMP}} = 0.054 A^{5/3}\ [\hbar^2\,\text{MeV}^{-1}], \quad (18)$$

together with the ATDHF collective energy correction. Note that Eq. (18) is obtained using the nuclear deformation parameter ϵ, whereas in the present study, the deformation is parametrized by the quadrupole Q_{20} deformation. A change of variable is thus needed to obtain the constant effective inertia $\mu_{Q_{20}}^{\text{SEMP}}$ within the Q_{20} coordinate framework. The relationship between nuclear deformation ϵ and quadrupole deformation

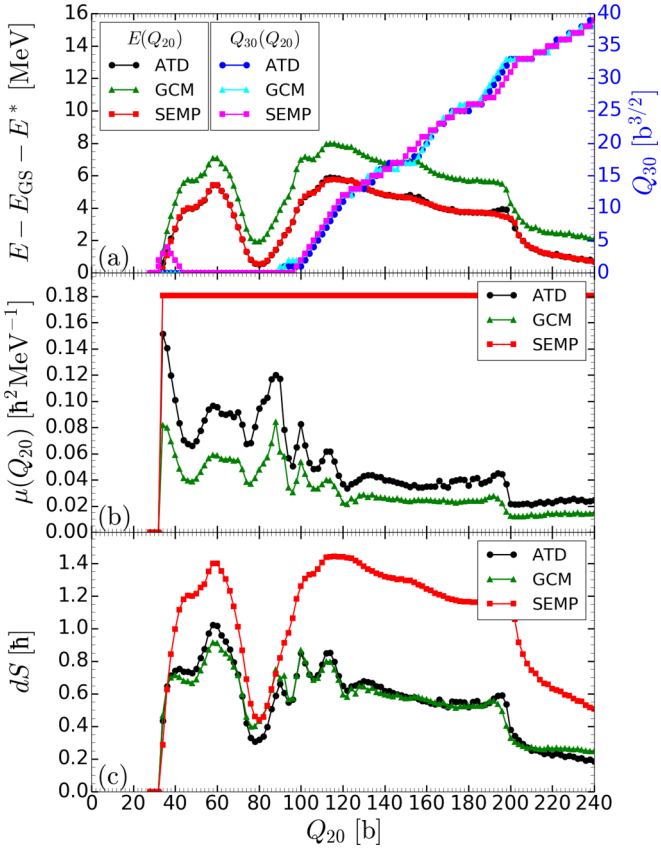

FIG. 9. (a)^{236}U LAP calculated for $E^* = E_{0^+}$ and different inertia, namely, ATD, GCM, and SEMP. (b) Effective inertia along the LAP. (c) Distance dS between two neighboring deformation points of the LAP. We have $S_{ATD} = 63.3\hbar$, $S_{GCM} = 66.7\hbar$, and $S_{SEMP} = 122.6\hbar$. The black curve in (a) is hidden by the red one.

Q_{20} is given to first leading term by [39]

$$\epsilon = \frac{5}{4AR_0^2} Q_{20}. \tag{19}$$

Using Eqs. (16), (18), and (19), the expression of $\mu_{Q_{20}}^{SEMP}$ reads

$$\mu_{Q_{20}}^{SEMP} = 0.04069 A^{-5/3} \ [\hbar^2\,\mathrm{MeV}^{-1}\,\mathrm{fm}^{-4}]. \tag{20}$$

As shown in Fig. 9, the SEMP inertia is significantly higher than in the GCM or ATDHF framework, leading inevitably to higher action along the fission path. The resulting SEMP action for a constant inertia LAP amounts to 122.6ħ, which is very different from the ATDHF or GCM one.

V. COMPARISON BETWEEN LEP AND LAP

The LEP and LAP for ^{226}Th and ^{238}U are compared in Figs. 10 and 11, respectively. These two cases, previously studied in Ref. [17], show different behaviors of the LAP with respect to the LEP.

The ^{226}Th LAP is found to be significantly different from its LEP (Fig. 10). The fission barrier of the LAP is higher by about 4 MeV than the LEP barrier, the action, however, being lower due to the effect of the inertia tensor. More specifically, for $120 < Q_{20}$ [b] < 200 deformations, the inertia along the

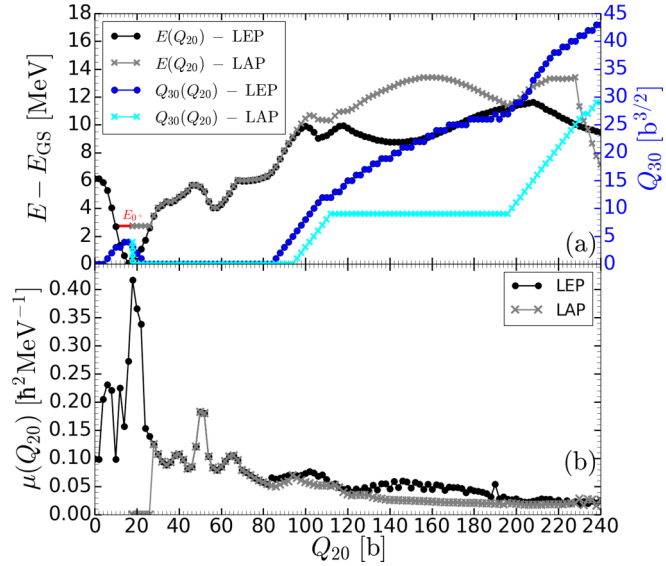

FIG. 10. (a) Energy $E(Q_{20})$ (left y-axis scale) and mass asymetry $Q_{30}(Q_{20})$ (right y-axis scale) of the LEP and LAP of ^{226}Th calculated with $E^* = E_{0^+} = 2.7$ MeV. (b) ATDHF inertia along the LEP and LAP.

LAP is twice as small relative to that along the LEP, though the energy along the LAP is about 1.5 times higher on average. As the action between two neighboring points dS depends on the product between the inertia $\mu(x)$ and $V - E$ [see Eq. (17)], the LAP differs from the LEP. The ^{226}Th LAP is globally less asymmetric than its LEP, mainly for $Q_{20} > 110$ b, whereas the LEP becomes more and more asymmetric with increasing Q_{20} due to the presence of a well at $(Q_{20}$[b], Q_{30}[b$^{3/2}$]$) = (146, 22)$ after the saddle point located at (108,15). The

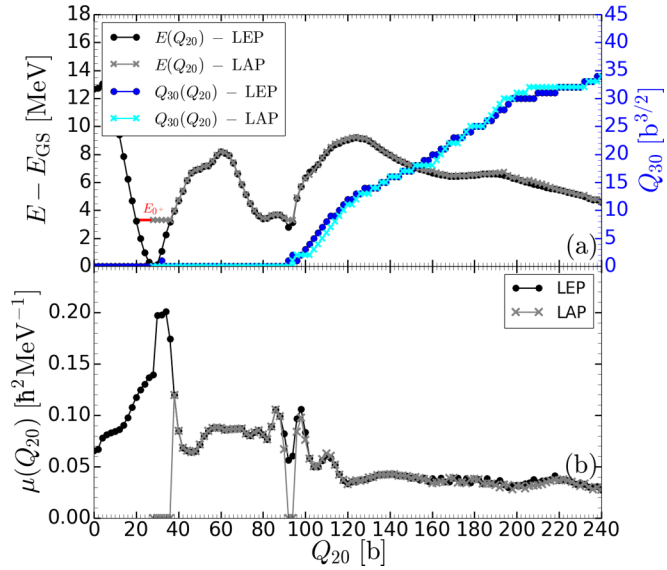

FIG. 11. (a) Energy $E(Q_{20})$ (left y-axis scale) and mass asymetry $Q_{30}(Q_{20})$ (right y-axis scale) of the LEP and LAP of ^{238}U calculated with $E^* = E_{0^+} = 3.3$ MeV. (b) ATDHF inertia along the LEP and LAP.

asymmetry of the LAP remains constant between $Q_{20} = 112$ b and $Q_{20} = 196$ b even if the potential energy is higher along this part of the LAP compared to the LEP within the same Q_{20} range because an increase in Q_{30} at a given point is less favorable from an inertia point of view. Indeed, according to (16), the inertia along the Q_{20} direction is equal to

$$\mu_{Q_{20}}(x) = B_{22}\left(\frac{dQ_{20}}{dx}\right)^2, \tag{21}$$

whereas along the $Q_{20} + Q_{30}$ direction, it reads

$$\mu_{Q_{20}+Q_{30}}(x) = B_{22}\left(\frac{dQ_{20}}{dx}\right)^2 + 2B_{23}\frac{dQ_{20}}{dx}\frac{dQ_{30}}{dx} + B_{33}\left(\frac{dQ_{30}}{dx}\right)^2. \tag{22}$$

Since $\mu_{Q_{20}+Q_{30}} > \mu_{Q_{20}}$ for $Q_{30} < 10\ \mathrm{b}^{3/2}$ in the ^{226}Th and ^{238}U cases, the Q_{20} direction is favored with respect to the $Q_{20} + Q_{30}$ direction as long as $Q_{30} < 10\ \mathrm{b}^{3/2}$. This effect can be counterbalanced by a large energy decrease, like the presence of a deep valley, enabling exploration of the $Q_{30} > 10\ \mathrm{b}^{3/2}$ region, where the $Q_{20} + Q_{30}$ direction is more favorable than the Q_{20} one.

Contrary to the ^{226}Th case, the ^{238}U LAP is almost identical to its LEP (Fig. 11). The inertias along the LAP and LEP are also almost identical. This is due to the presence of a deep and narrow valley after the saddle point (Q_{20}[b], Q_{30}[b$^{3/2}$]) = (124, 13). It is the energetic component of the action [Eq. (15)] which drives the LAP, whereas in the ^{226}Th case, the LAP results from a compromise between the potential energy and the inertia because the valley after the saddle point is not deep enough.

By increasing the excitation energy while keeping the same starting deformation point for the LAP, i.e., the ground state, the balance between the potential energy and the inertia can be modified. This is illustrated for the ^{226}Th case in Fig. 12. Areas without the tunneling effect, i.e., $V < E$, do not contribute to the action [Eq. (15)]. There is an excitation energy threshold at which the LAP changes from the low-energy ($E^* = E_{0^+}$) regime found in the spontaneous fission LAP to the high-energy regime where the LAP becomes close to the LEP. This transition energy is found around 5.1 MeV as illustrated in Fig. 12. There is, however, no sudden modification of the action, which goes from 52.1$\hbar$ for $E^* = 5.1$ MeV to 51.1$\hbar$ for $E^* = 5.2$ MeV. More generally, the LAP's action decreases linearly and smoothly with increasing excitation energies, as shown in Fig. 13. The LAP tends to the LEP for an excitation energy $E^* = E_{\mathrm{barr,LEP}}$ corresponding to the highest saddle point of the LEP, since at this energy, there is no more tunneling effect during the fission process and the action drops to zero.

VI. SPONTANEOUS FISSION LIFETIMES

The spontaneous fission half-life can be obtained from the WKB formalism [40] as

$$T^{\mathrm{sf}}_{1/2}[\mathrm{s}] = 2.86 \times 10^{-21}(1 + e^{2S(E^*)/\hbar}), \tag{23}$$

where S is the action along the LAP computed with an excitation energy equal to the energy of the 0^+ ground-state

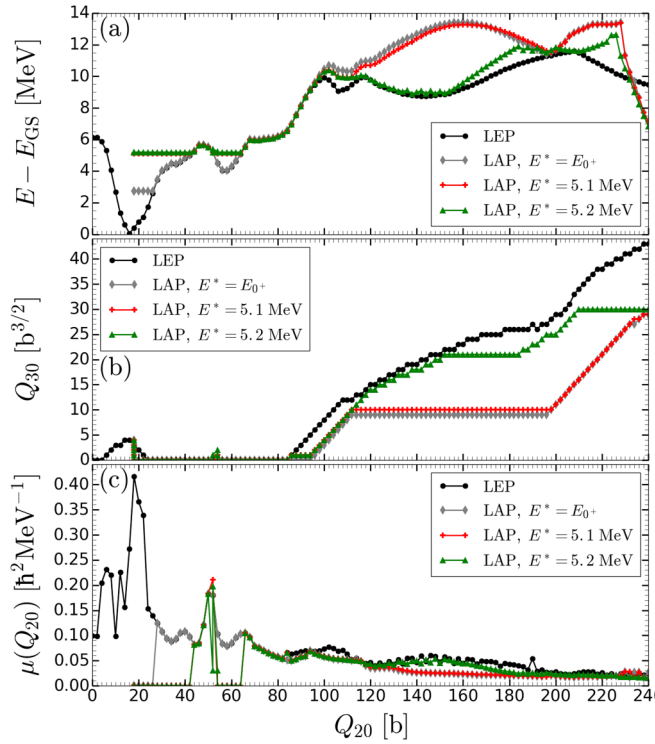

FIG. 12. (a) Energy, (b) mass asymetry Q_{30}, and (c) inertia of ^{226}Th LEP and LAP calculated with $E^* = E_{0^+} = 2.4$, 5.1, and 5.2 MeV.

level, since nuclei are expected to fission spontaneously from their fundamental 0^+ level, as mentioned in Sec. IV. The resulting half-lives are computed with the ATDHF and GCM LAPs and compared with experimental data in Fig. 14. Experimental half-lives are fairly well reproduced with the ATDHF LAP, though systematically overestimated. GCM LAPs tend to overestimate the half-lives even more. The short half-lives (typically $T^{\mathrm{sf}}_{1/2} \lesssim 1$ y) for nuclei with $Z \gtrsim 100$ are satisfactorily estimated. It is well known that fission half-lives are extremely sensitive to the adopted excitation energy E^*. To test this sensitivity, half-lives are also computed assuming that the excitation energy of the 0^+ level is underestimated by 0.5 MeV,

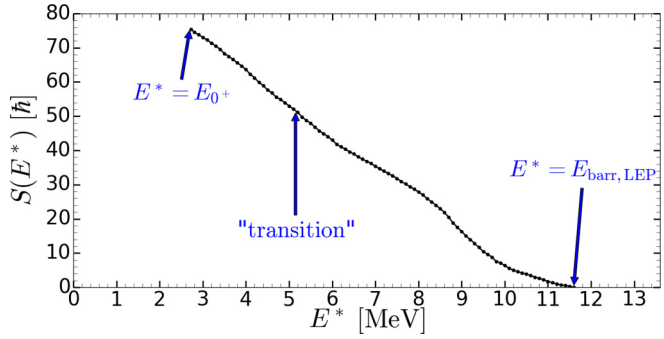

FIG. 13. LAP's action of ^{226}Th depending on the excitation energy, from E_{0^+} to the fission barrier height of the LEP $E_{\mathrm{barr,LEP}}$. The arrow at 5 MeV refers to the transition of the LAP between an akin to spontaneous fission LAP to an akin to LEP.

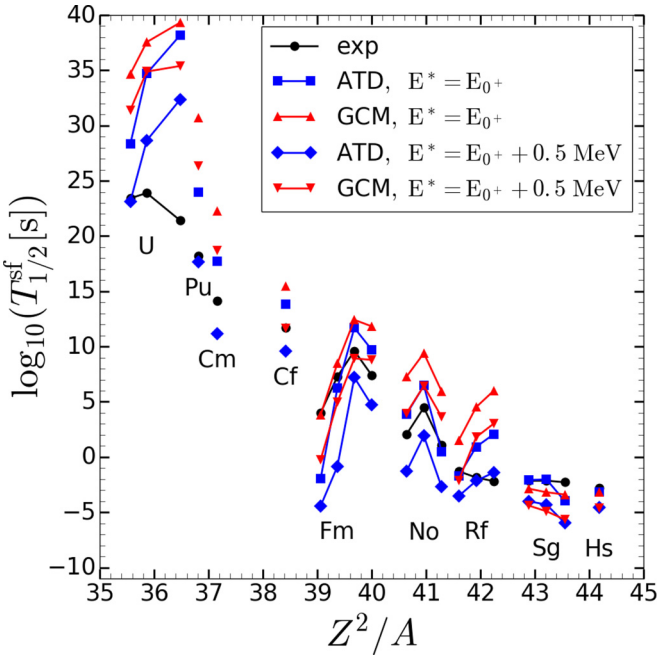

FIG. 14. Spontaneous fission half-lives $T^{sf}_{1/2}$ obtained for $^{232-238}$U, ^{240}Pu, ^{248}Cm, $^{250-256}$Fm, $^{252-256}$No, $^{256-260}$Rf, $^{258-262}$Sg, and ^{264}Hs as a function of the fissibility parameter Z^2/A with $E^* = E_{0^+}$ and $E^* = E_{0^+} + 0.5$ MeV. Results were obtained with either the ATDHF or the GCM correction. Theoretical results are compared with experimental data [41].

i.e., $E^* = E_{0^+} + 0.5$ MeV. The corresponding predictions are shown in Fig. 14. Half-lives vary by two to three orders of magnitude for heavy nuclei and up to five orders of magnitude for U isotopes.

VII. CONCLUSION

The LEP and LAP have been obtained for a large number of nuclei using the Gogny D1M PES, where triaxial and collective corrections are included. LEPs were computed with an improved flooding method using a binary search tree data structure to avoid drawbacks of the iterative method when there is a shape isomer. The fission barriers deduced from the LEP are in good agreement with evaluated data. Our systematic study of the fission barrier has confirmed that nuclear shell structures have an impact on the fission barrier height but no impact on the location of the highest saddle point along the LEP. Close to the $N = 184$ neutron shell closure, the fission barrier height increases. To calculate spontaneous fission lifetimes in the WKB approximation, the actions of the LAP are needed. They have been computed with Dijkstra's minimization algorithm. A comparative study between ^{226}Th and ^{238}U shows that the LEP and LAP are similar or very different depending on the PES landscape and, more particularly, on the depth of the valleys. A transition in LAP shape was observed for ^{226}Th, but without any impact on the action evolution with the excitation energy, which decreases linearly. The spontaneous fission lifetimes are fairly well reproduced using the ATDHF framework but their predictions are very sensitive to the excitation energy of the fissioning nucleus. It is planned to extend our LEP and LAP calculations systematically to odd nuclei, which will be challenging due to quasiparticle level blocking issues.

ACKNOWLEDGMENTS

Useful discussions with M. Meyer about Dijkstra's algorithm are gratefully acknowledged. This work was possible thanks to funding from the F.R.S.-FNRS (Belgium).

[1] D. Kasen, B. Metzger, J. Barnes, E. Quataert, and E. Ramirez-Ruiz, Nature **551**, 80 (2017).
[2] M. Arnould, S. Goriely, and K. Takahashi, Phys. Rep. **450**, 97 (2007).
[3] S. Goriely, J.-L. Sida, J.-F. Lemaître, S. Panebianco, N. Dubray, S. Hilaire, A. Bauswein, and H.-T. Janka, Phys. Rev. Lett. **111**, 242502 (2013).
[4] O. Just, A. Bauswein, R. A. Pulpillo, S. Goriely, and H.-T. Janka, MNRAS **448**, 541 (2015).
[5] S. Bjørnholm and J. E. Lynn, Rev. Mod. Phys. **52**, 725 (1980).
[6] S. Goriely, M. Samyn, and J. M. Pearson, Phys. Rev. C **75**, 064312 (2007).
[7] S. Goriely, S. Hilaire, M. Girod, and S. Péru, Phys. Rev. Lett. **102**, 242501 (2009).
[8] S. A. Giuliani, L. M. Robledo, and R. Rodríguez-Guzmán, Phys. Rev. C **90**, 054311 (2014).
[9] R. Rodríguez-Guzmán and L. M. Robledo, Phys. Rev. C **89**, 054310 (2014).
[10] J.-F. Lemaître, S. Panebianco, J.-L. Sida, S. Hilaire, and S. Heinrich, Phys. Rev. C **92**, 034617 (2015).
[11] S. Panebianco, J.-L. Sida, H. Goutte, J.-F. Lemaître, N. Dubray, and S. Hilaire, Phys. Rev. C **86**, 064601 (2012).
[12] K.-H. Schmidt and B. Jurado, Phys. Rev. C **83**, 061601 (2011).
[13] J.-P. Delaroche, M. Girod, H. Goutte, and J. Libert, Nucl. Phys. A **771**, 103 (2006).
[14] J. Berger, M. Girod, and D. Gogny, Nucl. Phys. A **428**, 23 (1984).
[15] J. Berger, M. Girod, and D. Gogny, Comput. Phys. Commun. **63**, 365 (1991).
[16] M. Bender, P.-H. Heenen, and P.-G. Reinhard, Rev. Mod. Phys. **75**, 121 (2003).
[17] A. Dobrowolski, H. Goutte, and J.-F. Berger, Int. J. Mod. Phys. E **16**, 431 (2007).
[18] H. Goutte, J. F. Berger, P. Casoli, and D. Gogny, Phys. Rev. C **71**, 024316 (2005).
[19] N. Dubray and D. Regnier, Comput. Phys. Commun. **183**, 2035 (2012).
[20] S. Hilaire and M. Girod, Eur. Phys. J. A **33**, 237 (2007), and references therein.
[21] M. Girod and B. Grammaticos, Phys. Rev. Lett. **40**, 361 (1978).
[22] J. Berger and D. Gogny, Nucl. Phys. A **333**, 302 (1980).
[23] M. Girod and B. Grammaticos, Phys. Rev. C **27**, 2317 (1983).
[24] L. Bonneau, P. Quentin, and D. Samsœn, Eur. Phys. J. A **21**, 391 (2004).
[25] J. Libert, M. Girod, and J.-P. Delaroche, Phys. Rev. C **60**, 054301 (1999).
[26] B.-N. Lu, J. Zhao, E.-G. Zhao, and S.-G. Zhou, Phys. Rev. C **89**, 014323 (2014).

[27] P. Ring and P. Schuck, *The Nuclear Many-Body Problem. Physics and Astronomy Online Library* (Springer, Berlin, 2004).
[28] M. Girod and B. Grammaticos, Nucl. Phys. A **330**, 40 (1979).
[29] A. Mamdouh, J. Pearson, M. Rayet, and F. Tondeur, Nucl. Phys. A **644**, 389 (1998).
[30] A. Drozdek, *Data Structures and Algorithms in C++*, 4th ed. (Cengage Learning, Boston, MA, 2012).
[31] R. Capote, M. Herman, P. Obložinský, P. Young, S. Goriely, T. Belgya, A. Ignatyuk, A. Koning, S. Hilaire, V. Plujko, M. Avrigeanu, O. Bersillon, M. Chadwick, T. Fukahori, Z. Ge, Y. Han, S. Kailas, J. Kopecky, V. Maslov, G. Reffo, M. Sin, E. Soukhovitskii, and P. Talou, Nucl. Data Sheets **110**, 3107 (2009).
[32] P. Möller, A. J. Sierk, T. Ichikawa, A. Iwamoto, R. Bengtsson, H. Uhrenholt, and S. Åberg, Phys. Rev. C **79**, 064304 (2009).
[33] A. Baran, K. Pomorski, A. Lukasiak, and A. Sobiczewski, Nucl. Phys. A **361**, 83 (1981).
[34] P. Demetriou, M. Samyn, and S. Goriely, in *Seminar on Fission, Pont d'Oye V*, edited by C. Wagemans, J. Wagemans, and P. D'Hondt (World Scientific, Singapore, 2004), pp. 21–28.
[35] M. Brack, J. Damgaard, A. S. Jensen, H. C. Pauli, V. M. Strutinsky, and C. Y. Wong, Rev. Mod. Phys. **44**, 320 (1972).
[36] D. Regnier, N. Dubray, N. Schunck, and M. Verrière, Phys. Rev. C **93**, 054611 (2016).
[37] E. W. Dijkstra, Numer. Math. **1**, 269 (1959).
[38] J. D. Cramer and J. R. Nix, Phys. Rev. C **2**, 1048 (1970).
[39] R. Hasse and W. Myers, *Geometrical Relationships of Macroscopic Nuclear Physics*, Springer Series in Nuclear and Particle Physics (Springer-Verlag, Berlin, 1988).
[40] S. G. Nilsson, C. F. Tsang, A. Sobiczewski, Z. Szymański, S. Wycech, C. Gustafson, I.-L. Lamm, P. Möller, and B. Nilsson, Nucl. Phys. A **131**, 1 (1969).
[41] N. E. Holden and D. C. Hoffman, Pure Appl. Chem. **72**, 1525 (2000).